Varying Magnus effect on a rotating sphere at intermediate Reynolds numbers

Anchal Sareen [a],[*], Kerry Hourigan [b], Mark C. Thompson [b]

[a] Department of Naval Architecture and Marine Engineering, Mechanical Engineering, University of Michigan, Ann Arbor, USA
[b] Fluids Laboratory for Aeronautical and Industrial Research (FLAIR), Department of Mechanical and Aerospace Engineering, Monash University, Melbourne, VIC 3800, Australia

ARTICLE INFO

ABSTRACT

Rotating bluff bodies are known to experience a side force due to a well-known phenomenon called the Magnus effect. The Magnus effect is evident in many sports (cricket, soccer, baseball, and football), where spinning balls are observed to change their trajectories dramatically. In this paper, we have experimentally investigated the effect of imposed transverse rotation on flow past a sphere in the intermediate Reynolds number range ($10^3 < Re \lesssim 5 \times 10^4$). The results show the considerable effects of Reynolds number and the rotation rate on the force coefficients. A relatively sudden drop was observed in both the lift and drag coefficients at a 'critical' rotation rate, before a recovery at higher values, similar to but lower in magnitude than that observed near the drag crisis Reynolds number range ($Re \approx 3 \times 10^5$). The change in lift was found to be correlated with the change in the separation angle on the advancing side of the sphere, which occurs when the boundary layer flow becomes unsteady and turbulent, presumably as a result of the shear-layer instability observed for rotating spheres. The situation appears to be similar at lower Reynolds number ($Re < 1000$), with early transition to boundary layer turbulence causing the advancing side separation angle to increase substantially at a critical rotation rate. However, the boundary layer thickness is considerably thicker at lower Reynolds number, which presumably limits its ability to remain attached to high angles thus limiting the magnitude of the effect. Of interest, the shear-layer instability that develops as the rotation rate is increased manifests even at very low Reynolds numbers, suggesting that the origins of the inverse Magnus effect may be observable at even lower Reynolds numbers than those studied here.

1. Introduction

Fluid–structure interaction of rotating bluff bodies has intrigued scientists for centuries. It finds applications not only in sports where spinning balls are known to change trajectories but also in ship propulsion (Flettner rotors), external ballistics, particle-laden flows, saltation of particles, and aeronautic applications. Rotating bluff bodies are known to experience a side force (the Magnus force) due to a well-known phenomenon called the Magnus effect, which is a consequence of the asymmetry of flow separation on the advancing and retreating sides of a rotating body. The sphere, the three-dimensional body with the highest symmetry, represents an ideal body to investigate the flow physics further before tackling the more complex bodies that surround us. Interestingly, the discovery of the Magnus effect for a sphere occurred almost two centuries earlier than that of its two-dimensional counterpart, the circular cylinder. However, there have been fewer experimental studies on rotating spheres due to the challenges of developing experimental setups and drive systems that do not unduly interfere with the flow over them.

Most of the previous literature on transversely rotating spheres can be broadly classified into two groups: the first set of studies are mostly numerical studies that focused on low Reynolds numbers of $Re \leq 1000$ (e.g., Poon et al. (2010), Loth (2008), Tanaka et al. (1990), Tsuji et al. (1985)). The second set of studies are mostly experimental studies that focused on very high Reynolds numbers of $Re \geq 6 \times 10^4$ (e.g., (Macoll, 1928; Barlow and Domanski, 2008; Kray et al., 2012; Kim et al., 2014; Rooney et al., 2022; Ward et al., 2020; Li et al., 2023b,a; Ward et al., 2023)). These sets of studies found different characteristic drag and lift profiles for varying rotation rates (also shown in Fig. 1). Studies performed at low Reynolds numbers showed a monotonic increase in the force coefficients with the rotation rate α. However, the studies performed at high Reynolds numbers have focused mainly on the *inverse Magnus effect*, where one observes a sudden change in the
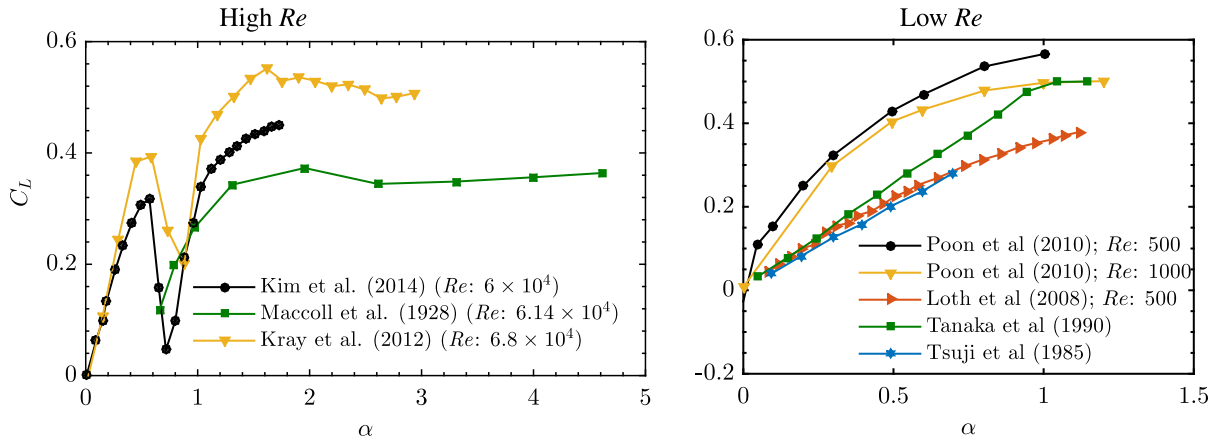
Fig. 1. Variation of the lift coefficient C_L with the rotation ratio α for previous studies showing inconsistencies in the reported data for similar Reynolds numbers. Left: High Reynolds numbers experimental studies. Right: Low Reynolds numbers studies.

direction of the lift force at a 'critical' rotation ratio. They observed the inverse Magnus effect for a narrow range of rotation ratios at very high Reynolds numbers ($Re \geq 8 \times 10^4$), close to the drag crisis range for a non-rotating sphere. The question arises as to what the force coefficients look like in the intermediate Reynolds number range ($10^3 < Re \lesssim 5 \times 10^4$). Do the coefficients increase monotonically similar to that reported for low Reynolds numbers or is there a sudden drop in the coefficients, similar to that observed at high Reynolds numbers? Also, what are the underlying dynamics? These questions remain unanswered. Moreover, the small magnitude of forces for intermediate Reynolds numbers make measurements challenging, at least in low viscosity working fluids such as water and air. This is the reason many previous experimental studies on rotating spheres have been focused on higher Reynolds numbers in spite of the relevance of intermediate Reynolds numbers to many engineering applications, such as particle flows where particle–particle and particle–wall collisions can lead to combined translational and rotational motion of the spherical particles. Moreover, due to difficulty of measuring quantitatively the flow near the surface of a rotating sphere, the details behind the Magnus effect are not well understood. Recently, lifting devices using the Magnus effect have received attention due to their high lift forces and stall resistance. This interest remains current in spite of the added complexity of the driving mechanisms. It is crucial to know the rotation rates for which the forces suddenly drop for more effective and safer designs. Therefore, in the current paper, the effect of the rotation ratio on the drag and lift profiles of a sphere is studied for intermediate Reynolds numbers. Flow-visualisations using Fluorescein dye and Particle Image Velocimetry measurements were also performed to understand the underlying dynamics.

The aerodynamic forces on a spinning sphere, the drag (F_D) and lift (F_L) forces, depend on various flow parameters such as density ρ, viscosity μ, sphere diameter D, and sphere angular velocity ω. From dimensional analysis, we obtain:

$$Re = \frac{\rho U D}{\mu}, \tag{1}$$

$$\alpha = \frac{D\omega}{2U}, \tag{2}$$

$$C_D, C_L = f(Re, \alpha), \tag{3}$$

where the drag and lift coefficients, C_D and C_L, are defined as follows:

$$C_D = \frac{F_D}{\frac{1}{2}\rho U^2 A}, \tag{4}$$

$$C_L = \frac{F_L}{\frac{1}{2}\rho U^2 A}, \tag{5}$$

where A is sphere projected area ($A = \pi D^2/4$).

2. Experimental arrangement

The experiments were conducted in the recirculating free-surface water channel of the Fluids Laboratory for Aeronautical and Industrial Research (FLAIR), Monash University, Australia. The test section of the channel is 600 mm in width, 800 mm in depth and 4000 mm in length. The free stream velocity can be varied in the range of $0.05 \leq U^* \leq 0.45$ ms^{-1}. The free stream turbulence levels in the test section were less than 1% over the velocity range studied. The spherical model used was 80 mm in diameter, with a smooth surface finish. It was supported from the top apex using a cylindrical support rod. To reduce interference, the driving shaft (3 mm in diameter) was covered with a fixed cylindrical shroud, 6.35 mm in diameter. The sphere was placed more than 2 diameters beneath the free surface to minimise any free-surface effects. Prior study by Sareen et al. (2018c) found that the free surface has no substantial effect on the flow past a sphere when the distance between the free surface and the top of the sphere is more than one sphere diameter.

To drive the sphere over a range of rotational speeds, a miniature low-voltage LV172 Parker stepper motor was used. It was controlled using a Parker 6K controller. The vibration of the sphere due to rotation was minimised by adopting a very stiff fixed support shaft supported by miniature ball bearings at the end. More details of the support setup and the rotation rig can be found in the related studies by Wong et al. (2017, 2018), Sareen et al. (2018a,c,b).

The forces acting on the sphere were measured using a multi-axis load cell (Mini40, ATI-IA), which measures six-component forces and moments (F_x, F_y, F_z, M_x, M_y, M_z) with a resolution of 0.005 N for F_x and F_y, and 0.01 N for F_z, respectively. For each data set, the raw analogue voltages were acquired at 100 Hz for 300 s at each flow velocity, and were converted to a digital signal using a differential-ended DAQ board system. Fluorescein dye was used for flow visualisations. The dye was injected using a pitot tube placed upstream of the sphere.

In order to estimate the flow separation location on the surface of sphere, 2D-2C PIV measurements were performed in the equatorial plane. For this purpose, the flow was seeded with 13 µm hollow microspheres having a specific weight of 1.1 gm^{-3}. Imaging was performed using a high-speed camera (model: Dimax S4, PCO, AG) with a resolution of 2016 × 2016 pixels^2. This camera was equipped with a 200 mm Nikon lens, giving a magnification of 34.28 pixel mm^{-1} for the field-of-view. For each PIV measurement case, a set of 3100 image pairs were sampled at 10 Hz. Velocity fields were deduced using in-house PIV software developed originally by Fouras et al. (2008), using 32 × 32 pixel^2 interrogation windows in a grid layout with 50% window overlap. The overall schematic of the experimental arrangement is shown in Fig. 2.
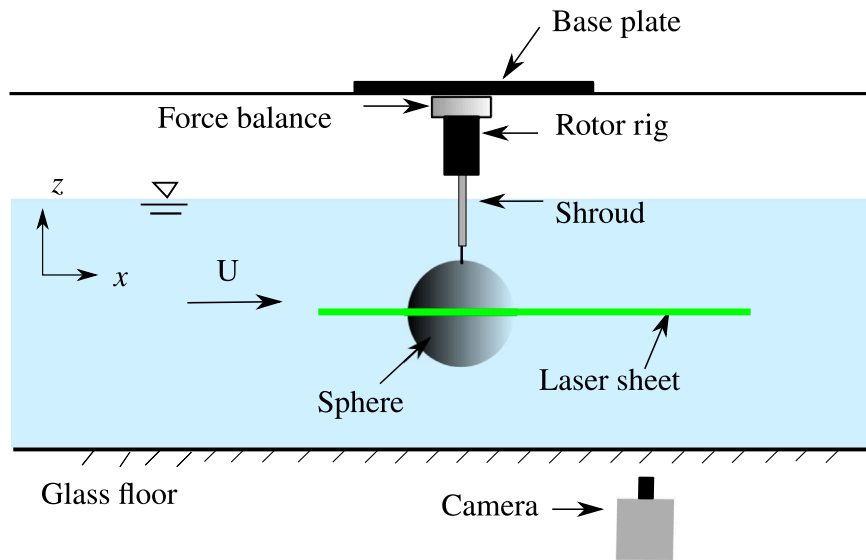
Fig. 2. Schematic showing the experimental arrangement (not to scale) for this study.
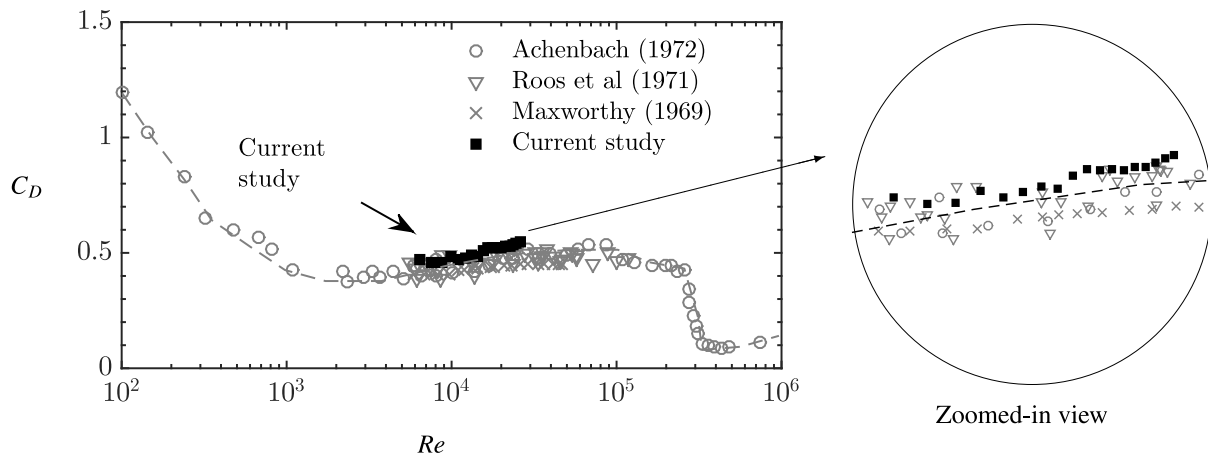

Fig. 3. Variation of the drag coefficient C_D of a stationary sphere with Reynolds number. Zoomed in view of the current results is shown on the right.
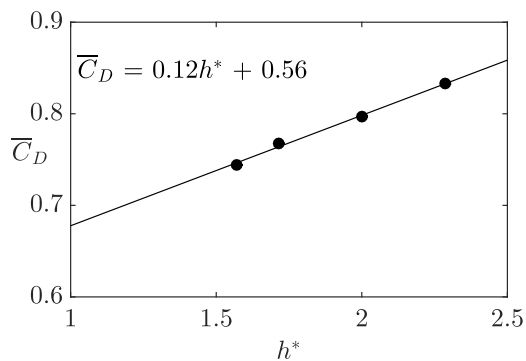

Fig. 4. Variation of $\overline{C}_D$ (averaged over the Re range) with the immersion depth for a sphere.

3. Stationary sphere validation

To verify the performance of the force balance in the current experimental arrangement, the Reynolds number dependent drag coefficient of a stationary sphere (70 mm in diameter) supported using a cylindrical support rod of diameter 6.35 mm was measured. The sphere upper surface was two diameters beneath the free surface. The force on the isolated support rod was measured after removing the sphere and correcting the end condition using an end plate. That force was subtracted from the measured force to correct the drag coefficient. Fig. 3 shows that the drag coefficient estimated in the current experimental arrangement collapses well and agrees with previous literature. It also suggests to reasonable accuracy that the force on the cylinder and sphere add approximately linearly to give the force on the rod/sphere combination. Another experiment was performed measuring drag coefficient for various non-dimensionalised immersion depths of the support rod (h^* = immersion depth/diameter of the sphere). As evident from Fig. 4, the drag coefficient varied linearly with the immersion depth, allowing an estimate of the mean drag coefficient by extrapolating to zero immersion depth. This experiment further demonstrated that the forces on the support rod and the sphere are at most only weakly coupled and that the estimated drag coefficients collapse well with those from previous studies.

As also highlighted in Fig. 3, the Reynolds number range for the current study lies in the 'subcritical' regime, where the drag coefficient stays reasonably constant for a wide range of Reynolds numbers. This intermediate Reynolds number regime is not well explored in the literature, as discussed in the previous section. Therefore, in the following sections, the effect of rotation on the flow past a sphere in the intermediate Reynolds number regime will be discussed in detail.

Results will be presented for representative Reynolds numbers cases in this regime.

4. Forces on a rotating sphere

In this section we will discuss the forces acting on a rotating sphere for representative Reynolds numbers. Fig. 5 shows the variation of the lift coefficient C_L, and the drag coefficient C_D, with the spin ratio α in all the three Reynolds number regimes for a selected set of Reynolds numbers. All the experiments were repeated at least three times and the random uncertainties are reported as standard deviation of the mean across the repetitions. As evident from the figure, the uncertainties are too small (of the order of the resolution of the force sensor). Hence, we drop the error bars in the rest of the reported data. Previous numerical study by Poon et al. (2014) performed at lower Reynolds numbers ($Re \leqslant 1000$) demonstrated a monotonic increase of lift and drag coefficients with the rotation ratio α, at least for $\alpha \leq 1$. However, the present study reveals a sharp drop in the force coefficients beyond a certain α value. When the Reynolds number is increased from 2.75×10^4 to 4.13×10^4 in the current study, only a small change is observed in C_L. However, C_D decreases significantly, and the 'critical' alpha value, where the sudden drop is observed, also decreases. The results are consistent with those from the previous experimental study at higher Reynolds numbers (Kim et al., 2014), which also revealed a sudden drop in the force coefficients, but for lower α values. One should note here that for very high Reynolds numbers of $Re \gtrsim 10^5$, the dip in coefficients become more dramatic, reaching negative C_L values for a certain range of α (Kim et al., 2014). For these rotational rates, the inverse Magnus effect is observed, where the lift force acts in the opposite direction to that predicted by the Magnus effect. Overall, one can see here that the critical α decreases with the increase in Reynolds number. Also, the sudden drop in the coefficients become progressively smaller in magnitude with the decrease in Reynolds number. Interestingly, even at $Re = 300$ in numerical studies both Dobson et al. (2014) and Rajamuni et al. (2018) report a slight dip in the drag coefficient beyond $\alpha = 2$. However, it is not clear that this can be attributed to the same mechanism operating at higher Reynolds numbers, but this is discussed further below.

These results together with those from previous studies reveal that the 'critical' spin ratio and the drop in force coefficients are Reynolds number dependent. The current study indicates the drop can even be observed at $Re = 2.75 \times 10^4$, almost an order of magnitude below the critical Reynolds number of a sphere of $Re_{crit} \simeq 2.3 \times 10^5$ (Achenbach, 1972).

It is worth mentioning here that although the previous experimental studies by Kim et al. (2014), (Macoll, 1928) and Kray et al. (2012) were performed for a similar Reynolds number of $\approx 6 \times 10^4$, there are large variations in the reported data, as evident from Fig. 1(a). Even at low Reynolds numbers, there are inconsistencies in the data reported by different studies, e.g., see Fig. 1(b). Because of these inconsistencies in the previously reported data, it was difficult to discern an overall trend in the variation of the force coefficients over a wide range of Reynolds numbers.

5. Physics of the varying magnus effect

To further understand the underlying physics behind the sudden dip in the coefficients, the flow was visualised using Fluorescein dye. Fig. 6 shows the top view of the dye visualisations for a sphere rotating in the anticlockwise direction for various spin ratios, but at a Reynolds number of $Re = 3510$ that is considerably lower than the range considered for the force measurements. This Reynolds number was chosen as the dye visualisations are much clearer, allowing the boundary layer transition to be more easily observed as α is increased. Similar transitions also occur for both higher (e.g. Kim et al., 2014) and lower (e.g. Dobson et al., 2014) Reynolds numbers. In these flow visualisations, the
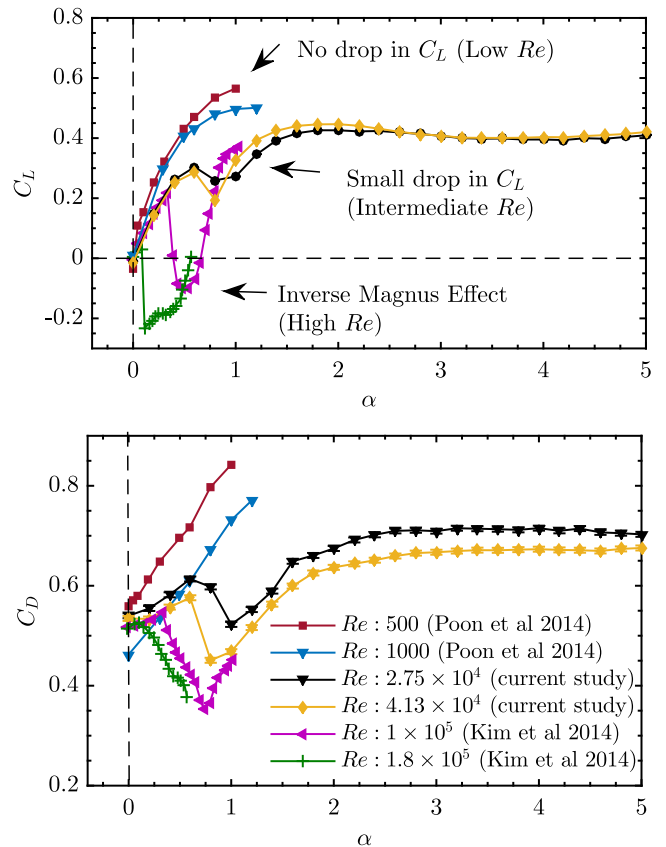

Fig. 5. Variation of the lift coefficient C_L (top) and the drag coefficient C_D (bottom) with the rotation ratio α for the current experiment compared to other studies at higher and lower Reynolds numbers. The error bars reported in the current data sets represent standard deviation of the mean across three repetitions.

flow is from left to right. We observe that as α changes from 0 to 0.2, the wake loses its symmetry and deflects in the direction of rotation, due to the Magnus effect. The wake deflects increasingly more with increasing α, correlated with an increasing Magnus force. At $\alpha = 1.5$, the boundary layer on the advancing side shows signs of turbulent transition that might be leading to separation delay due to increased crossflow momentum transport. At $\alpha = 3$, both the boundary layers become turbulent, and a further increase in rotation rate does not lead to any further increase in the force coefficients. Although these flow visualisation provides only qualitative picture of what is going on the wake of a rotating sphere, it is nevertheless very useful in visualising global wake deflection due to rotation. Particle image velocimetry results discussed in the following provide more quantitative estimation of the flow field and flow separation location.

To obtain a quantitative measure of the changes in the separation angles due to turbulent transition, Particle image velocimetry (PIV) was performed in the equatorial plane passing through the centre of the sphere. The wake past a rotating sphere is highly complex consisting of counter-rotating hairpin loops, as reported in the studies by Ward et al. (2020), Li et al. (2023b,a). The tomographic PIV measurements performed by Ward et al. (2020) revealed that the two vortices move in the direction of rotation under a conventional Magnus Effect and the angular position of these vortices matched well with the experienced side forces. Investigating flow separation very close to the surface of the sphere can shed light into the physical phenomenon leading to forces experience by the sphere. Previous studies near the critical Reynolds number have shown that the lift coefficient is directly related to the difference between the advancing and retreating side separation angles (see Kim et al. (2014)) for a transversely rotating sphere. The retreating
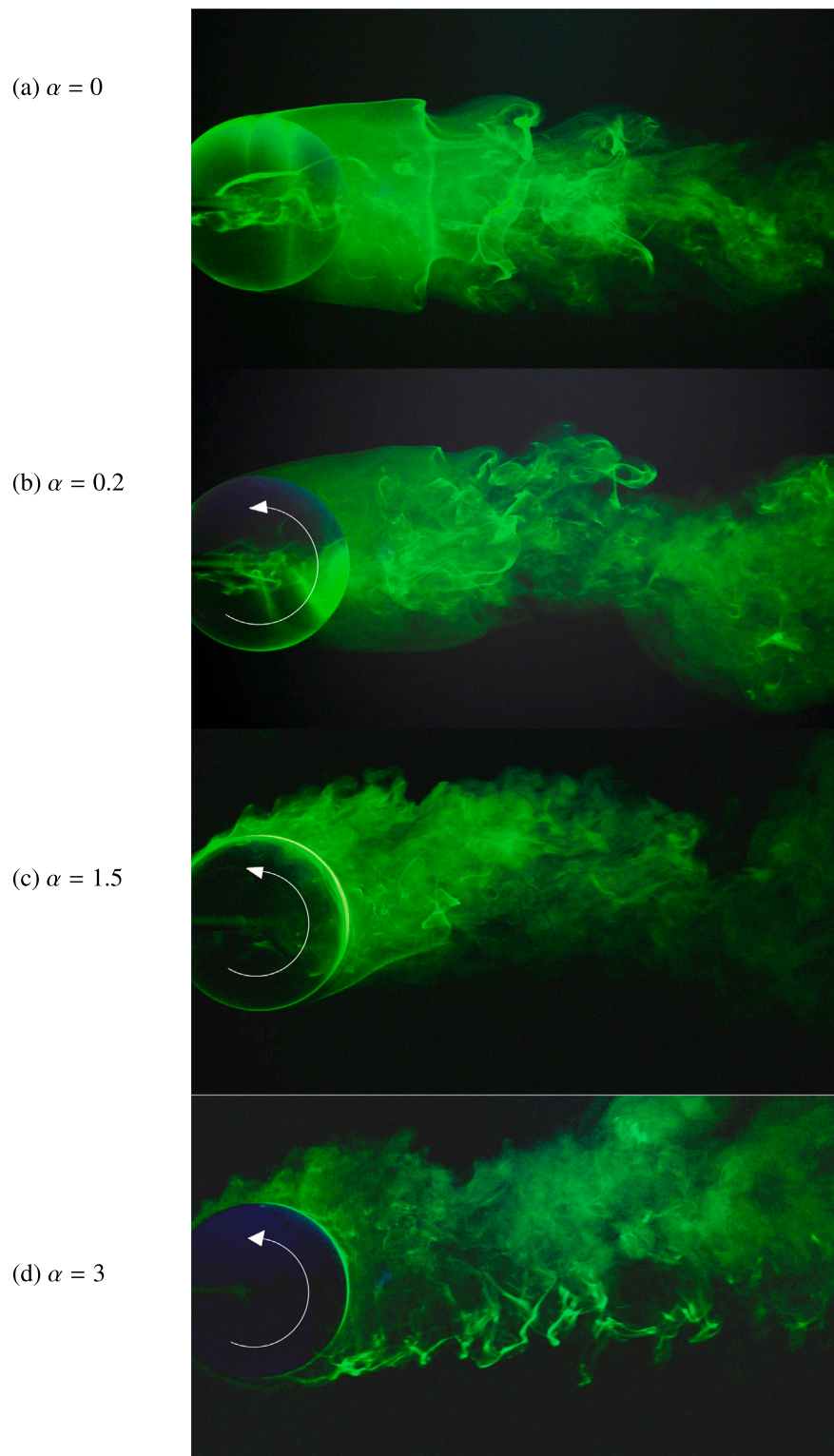
(a) $\alpha = 0$

(b) $\alpha = 0.2$

(c) $\alpha = 1.5$

(d) $\alpha = 3$

Fig. 6. Dye visualisation for a rotating sphere at $Re = 3510$ at marked spin ratios α. The figure shows the top view when the sphere is rotating in the anticlockwise direction and the flow is from left to right.

side separation angles increase linearly with the increase in the spin ratio. However, the variation of the advancing side separation angle (θ_{adv}) plays a key role in dictating the magnitude and direction of the lift force acting on the sphere. Hence, in the current study, the advancing side separation angles were estimated from the velocity fields based on the criterion: $u_\theta = 0$ and $\partial u_\theta / \partial r = 0$, where (r, θ) are polar coordinates with the origin at the centre of the sphere (e.g., see

Kim et al., 2014; Rott, 1956). The error in the estimation of the separation location is ± 1 degrees obtained by calculating the angle given by the interrogation window size considered in the PIV.

Fig. 7 shows time-averaged azimuthal velocity contours near the separation point at four different spin ratios. The flow separation at the advancing side of the sphere is clearly visible in the velocity contours. When the spin ratio is increased from $\alpha = 0.1$ to $\alpha = 0.4$,
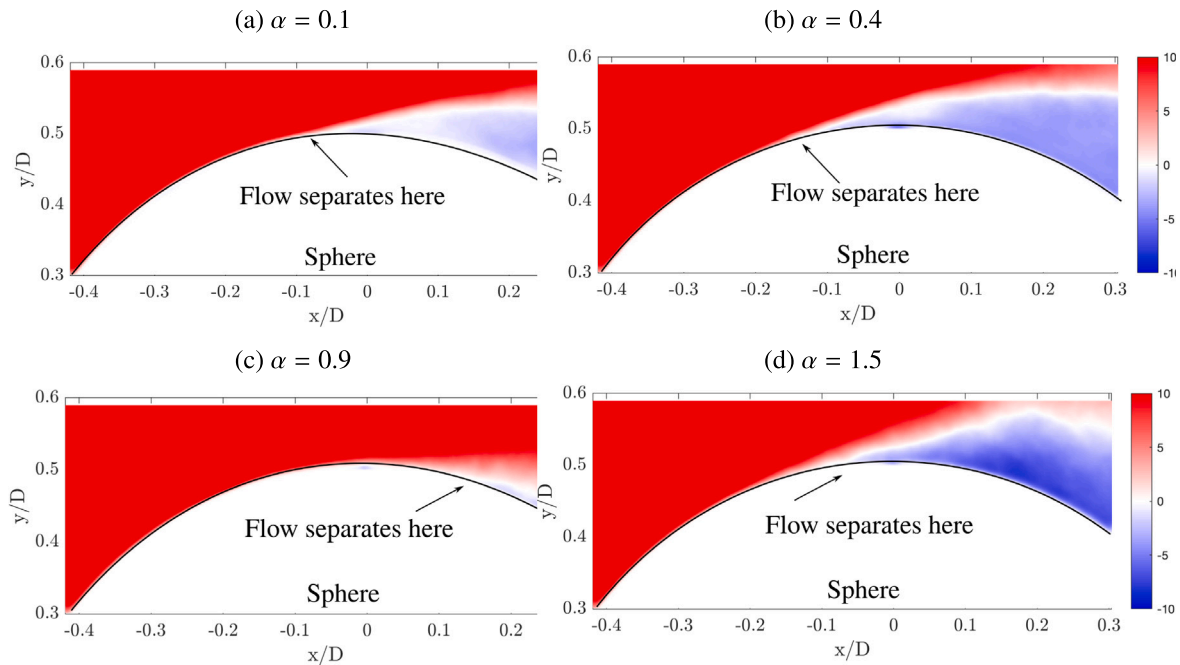
Fig. 7. Time-averaged azimuthal velocity contours near the flow separation at the advancing side of the sphere at (a) $\alpha = 0.1$, (b) $\alpha = 0.4$, (c) $\alpha = 0.9$ and (d) $\alpha = 1.5$. For this set of images, the flow is from left to right and the sphere rotates in the anticlockwise direction. The Reynolds number is 2.75×10^4. The white areas in the images represent negative velocity contours.

the separation angle clearly decreases. However, when the spin ratio is further increased to $\alpha = 0.9$, which lies in the critical regime, the flow reattaches to the sphere (Kim et al., 2014; Choi et al., 2008). This delays the flow separation at the advancing side of the sphere. With a further increase in the spin ratio to $\alpha = 1.5$, past the critical regime, the flow separation location moves upstream. It is conjectured her that the boundary layer transitions from laminar to turbulent and the flow separates without any reattachment.

Fig. 8 shows the variation of θ_{adv} with the spin ratio correlated with the variation of the lift coefficient. As evident from the figure, when the spin ratio is increased from 0 to ≈ 0.5, θ_{adv} decreases almost linearly. This bends the wake towards the advancing side of the sphere leading to an increased Magnus force towards the retreating side. A correlated increase in the lift coefficient is also evident in the figure. Beyond $\alpha = 0.5$, a sudden increase in the separation angle is observed correlated with a sudden drop in the lift coefficient. In the 'critical regime', the flow reattaches due to an increased momentum caused by transition to turbulence. This causes a delay in the flow separation that increases θ_{adv}. When α is further increased to higher values beyond the critical regime, θ_{adv} starts decreasing again and C_L starts increasing. At this stage the boundary layer on the retreating side becomes turbulent too. For very high rotation rates ($\alpha > 2$), both the boundary layers become turbulent (also seen in the dye visualisations in Fig. 6). There is no Magnus effect beyond this rotation ratio and hence, there is no further increase in the force coefficients. One can also infer here that for the Magnus effect to manifest, asymmetry in the boundary layers is required. If both the advancing and the retreating boundary layers are either laminar or turbulent, the Magnus effect is not observed.

6. Concluding remarks

This study has shown that even an order of magnitude below the critical Reynolds number, a sudden drop in the force coefficients is still observed with spin ratio (α), with the critical α and the magnitude of the drop in force coefficients dependent on the Reynolds number.

Flow visualisations reveal that the boundary layer on the advancing side becomes prematurely turbulent in the critical α regime, perhaps connected with the occurrence of the shear-layer instability (Poon et al., 2013), observed even at Reynolds numbers as low as $Re = 300$ (Dobson et al., 2014; Giacobello et al., 2009; Kim, 2009). However, for high spin ratios of $\alpha > 2$, both the advancing and retreating side boundary layers transition to turbulence, beyond which a further increase in coefficients are not observed. It is also shown using PIV measurements that there is a sudden increase in the advancing side separation angle in the critical regime, as observed at much higher Reynolds numbers (Kim et al., 2014), where the flow reattaches to the sphere and a small recirculation bubble is formed. For higher spin ratios the advancing side boundary layer becomes increasingly turbulent and the separation angle starts decreasing again. The current study reveals the underlying mechanism of the varying Magnus effect for intermediate Reynolds numbers, and serves as a bridge to connect the previous studies that were either performed for lower Reynolds numbers ($Re \leq 1000$) and much higher Reynolds numbers ($Re \geq 6 \times 10^4$).

From the current experiments, it is clear that in the intermediate Reynolds number range studied, smaller dips in the lift and drag co-efficients are still observed, which presumably translate directly to the inverse Magnus effect at higher Reynolds numbers. On this point, Kim et al. (2014) found that close to the critical Reynolds number and in the range $8 \times 10^4 \leq Re \leq 1.4 \times 10^5$, the size of the reduction in lift remained almost constant, while the shift in the advancing side separation angle approximately matched that observed for the separation angle of a non-rotating sphere at the drag crisis. At lower Reynolds numbers, this is not the case. The change in separation angle is considerably reduced, presumably consistent with the increased boundary layer thickness, which in turn, means that the ability of the boundary layer to remain attached to greater separation angles is reduced after the onset of the shear-layer instability. Thus, the present study helps elucidate the underlying principles of the varying Magnus effect as the Reynolds number approaches the critical regime.
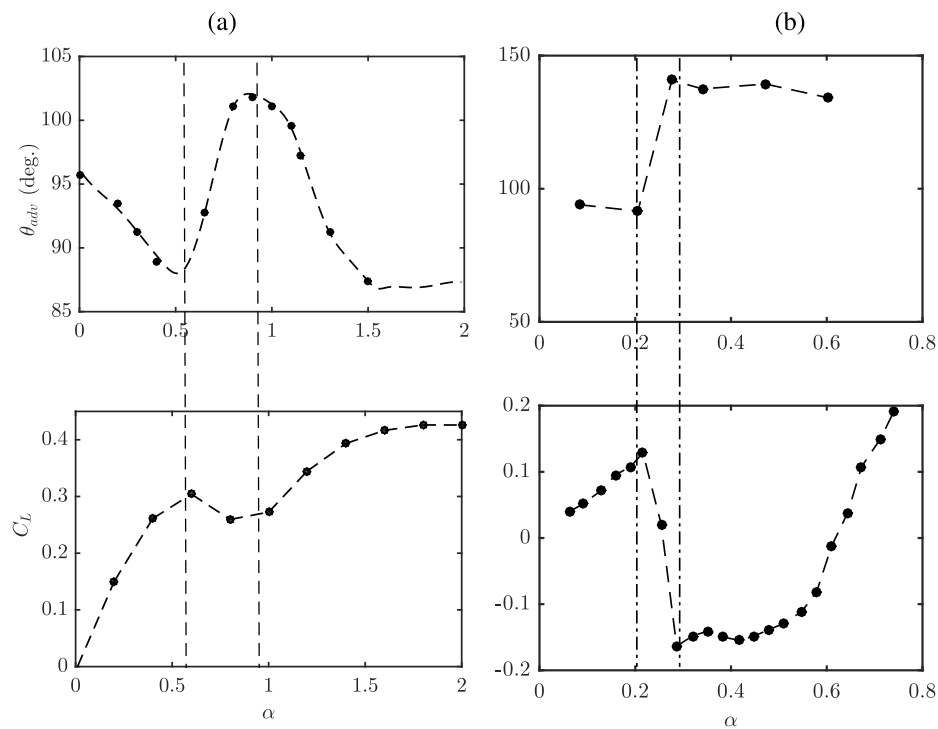
Fig. 8. Variation of the separation angle at the advancing side, θ_{adv}, with the rotation ratio α. The correlated transverse lift coefficient is also shown in the bottom. The dashed lines highlight the region where sudden increase in θ_{adv} is observed associated with a sudden drop in the lift coefficient. The figure on the right shows a similar curve reported by Kim et al. (2014) for a Reynolds number of 1.4×10^5.

CRediT authorship contribution statement

Anchal Sareen: Writing – review & editing, Writing – original draft, Visualization, Validation, Methodology, Investigation, Formal analysis, Data curation, Conceptualization. **Kerry Hourigan:** Writing – review & editing, Supervision, Resources, Project administration, Methodology, Investigation, Funding acquisition, Formal analysis, Conceptualization. **Mark C. Thompson:** Writing – review & editing, Supervision, Resources, Project administration, Methodology, Investigation, Funding acquisition, Formal analysis, Conceptualization.

Declaration of competing interest

The authors declare the following financial interests/personal relationships which may be considered as potential competing interests: Mark Thompson & Kerry Hourigan reports financial support was provided by Australian Research Council. If there are other authors, they declare that they have no known competing financial interests or personal relationships that could have appeared to influence the work reported in this paper.

Data availability

Data will be made available on request.

Acknowledgements

References

Achenbach, E., 1972. Experiments on the flow past spheres at very high Reynolds numbers. J. Fluid Mech. 54, 565–575.

Barlow, J.B., Domanski, M.J., 2008. Lift on stationary and rotating spheres under varying flow and surface conditions. AIAA J. 46 (8), 1932–1936.

Choi, H., Jeon, W., Kim, J., 2008. Control of flow over a bluff body. Annu. Rev. Fluid Mech. 40, 113–139.

Dobson, J., Ooi, A., Poon, E.W.K., 2014. The flow structures of a transversely rotating sphere at high rotation rates. Comput. & Fluids 102, 170–181.

Fouras, A., Lo Jacono, D., Hourigan, K., 2008. Target-free stereo PIV: a novel technique with inherent error estimation and improved accuracy. Exp. Fluids 44 (2), 317–329.

Giacobello, M., Ooi, A., Balachandar, S., 2009. Wake structure of a transversely rotating sphere at moderate Reynolds numbers. J. Fluid Mech. 621, 103–130.

Kim, D., 2009. Laminar flow past a sphere rotating in the transverse direction. J. Mech. Sci. Technol. 23 (2), 578–589.

Kim, J., Choi, H., Park, H., Yoo, J.Y., 2014. Inverse magnus effect on a rotating sphere: when and why. J. Fluid Mech. 754, R2.

Kray, T., Franke, J., Frank, W., 2012. Magnus effect on a rotating sphere at high Reynolds numbers. J. Wind Eng. Ind. Aerodyn. 110, 1–9.

Li, Z., Zhang, D., Liu, Y., Azma, A., Gao, N., 2023a. On the unsteady wake flow behind a sphere with large transverse-rotating speeds. Phys. Fluids 35 (10).

Li, Z., Zhang, D., Liu, Y., Gao, N., 2023b. Time-averaged flow field behind a transversely spinning sphere: An experimental study. Phys. Fluids 35 (3).

Loth, E., 2008. Lift of a spherical particle subject to vorticity and/or spin. AIAA J. (ISSN: 0001-1452) 46 (4), 801–809.

Macoll, J.W., 1928. Aerodynamics of a spinning sphere. J. R. Aeronaut. Soc. 28, 777–798.

Poon, E.K.W., Ooi, A.S.H., Giacobello, M., Cohen, R.C.Z., 2010. Laminar flow structures from a rotating sphere: effect of rotating axis angle. Int. J. Heat Fluid Flow 31 (5), 961–972.

Poon, E.W.K., Ooi, A.S.H., Giacobello, M., Cohen, R.C.Z., 2013. Hydrodynamic forces on a rotating sphere. Int. J. Heat Fluid Flow 42, 278–288.

Poon, E.K.W., Ooi, A.S., Giacobello, M., Iaccarino, G., Chung, D., 2014. Flow past a transversely rotating sphere at Reynolds numbers above the laminar regime. J. Fluid Mech. 759, 751–781.

Rajamuni, M.M., Thompson, M.C., Hourigan, K., 2018. Vortex-induced vibration of a transversely rotating sphere. J. Fluid Mech. 847, 786–820.

Rooney, D.M., Mortimer, P., Tricouros, F.A., Vaccaro, J.C., 2022. Wake flow measurements behind rotating smooth spheres and baseballs near critical Reynolds numbers. J. Fluids Eng. 144 (3), 031303.

Rott, N., 1956. Vortex-induced vibration of a transversely rotating sphere. Q. J. Appl. Math. 13, 444–451.

Sareen, A., Zhao, J., Lo Jacono, D., Sheridan, J., Thompson, M.C., 2018a. Vortex-induced vibration of a rotating sphere. J. Fluid Mech. 837, 258–292.

Sareen, A., Zhao, J., Sheridan, J., Hourigan, K., Thompson, M.C., 2018b. The effect of imposed rotary oscillation on the flow-induced vibration of a sphere. J. Fluid Mech. 855, 703–735.

Sareen, A., Zhao, J., Sheridan, J., Hourigan, K., Thompson, M.C., 2018c. Vortex-induced vibrations of a sphere close to a free surface. J. Fluid Mech. 846, 1023–1058.

Tanaka, T., Yamagata, K., Tsuji, Y., 1990. Experiment of fluid forces on a rotating sphere and spheroid. In: Proc. 2nd KSME-JSME Fluids Engineering Conference, Vol. 1. p. 366.

Tsuji, Y., Morikawa, Y., Mizuno, O., 1985. Experimental measurement of the magnus force on a rotating sphere at low Reynolds numbers. J. Fluids Eng. 107 (4), 484–488.

Ward, M., Passmore, M., Spencer, A., Hanson, H., Lucas, T., 2023. The effect of surface geometry on the aerodynamic behaviour of a football. Sports Eng. 26 (1), 33.

Ward, M., Passmore, M., Spencer, A., Harland, A., Hanson, H., Lucas, T., 2020. Comparing the aerodynamic behaviour of real footballs to a smooth sphere using tomographic PIV. In: Proceedings, Vol. 49, No. 1. MDPI, p. 150.

Wong, K.W.L., Zhao, J., Lo Jacono, D., Thompson, M.C., Sheridan, J., 2017. Experimental investigation of flow-induced vibration of a rotating circular cylinder. J. Fluid Mech. 829, 486–511.

Wong, K.W.L., Zhao, J., Lo Jacono, D., Thompson, M.C., Sheridan, J., 2018. Experimental investigation of flow-induced vibration of a sinusoidally rotating circular cylinder. J. Fluid Mech. 848, 430–466.